

UC Davis

UC Davis Previously Published Works

Title

Nanostructured complex oxides as a route towards thermal behavior in artificial spin ice systems

Permalink

<https://escholarship.org/uc/item/0345r61b>

Journal

Physical Review Materials, 1(2)

ISSN

2476-0455

Authors

Chopdekar, RV

Li, B

Wynn, TA

et al.

Publication Date

2017-07-01

DOI

10.1103/physrevmaterials.1.024401

Peer reviewed

PAPER

Engineered superlattices with crossover from decoupled to synthetic ferromagnetic behavior

To cite this article: Rajesh V Chopdekar *et al* 2018 *J. Phys.: Condens. Matter* **30** 015805

View the [article online](#) for updates and enhancements.

Engineered superlattices with crossover from decoupled to synthetic ferromagnetic behavior

Rajesh V Chopdekar¹, Vivek K Malik¹, Alexander M Kane¹,
Apurva Mehta², Elke Arenholz³ and Yayoi Takamura¹

¹ Department of Materials Science and Engineering, University of California, Davis, Davis, CA 95616, United States of America

² Stanford Synchrotron Radiation Lightsource, SLAC National Accelerator, Menlo Park, CA 94025, United States of America

³ Advanced Light Source, Lawrence Berkeley National Laboratory, Berkeley, CA 94720, United States of America

E-mail: ytakamura@ucdavis.edu

Received 11 August 2017, revised 5 November 2017

Accepted for publication 16 November 2017

Published 4 December 2017




CrossMark

Abstract

The extent of interfacial charge transfer and the resulting impact on magnetic interactions were investigated as a function of sublayer thickness in $\text{La}_{0.7}\text{Sr}_{0.3}\text{MnO}_3/\text{La}_{0.7}\text{Sr}_{0.3}\text{CoO}_3$ ferromagnetic superlattices. Element-specific soft x-ray magnetic spectroscopy reveals that the electronic structure is altered within 5–6 unit cells of the chemical interface, and can lead to a synthetic ferromagnet with strong magnetic coupling between the sublayers. The saturation magnetization and coercivity depends sensitively on the sublayer thickness due to the length scale of this interfacial effect. For larger sublayer thicknesses, the $\text{La}_{0.7}\text{Sr}_{0.3}\text{MnO}_3$ and $\text{La}_{0.7}\text{Sr}_{0.3}\text{CoO}_3$ sublayers are magnetically decoupled, displaying two independent magnetic transitions with little sublayer thickness dependence. These results demonstrate how interfacial phenomena at perovskite oxide interfaces can be used to tailor their functional properties at the atomic scale.

Keywords: superlattices, magnetic oxides, soft x-ray magnetic spectroscopy, interfaces

 Supplementary material for this article is available [online](#)

(Some figures may appear in colour only in the online journal)

Introduction

Due to the strong coupling between the charge, spin, orbital, and lattice degrees of freedom, perovskite oxides with the chemical formula ABO_3 display a wide range of technologically relevant properties including ferromagnetism, ferroelectricity, and superconductivity [1]. Modern thin film growth techniques such as pulsed laser deposition (PLD) offer atomic scale control of the chemical composition, structural properties, and thickness of sublayers, and therefore have enabled the engineering of artificial composite materials which display emergent properties which differ from those of the constituent materials [2, 3]. In these systems, interfacial interactions such

as structural effects (i.e. breaking the 3D symmetry of the material, epitaxial strain, and modifications of the inherent BO_6 octahedral tilts/rotations), chemical effects (i.e. atomic intermixing), electronic effects (i.e. electronic/orbital reconstruction, charge transfer), and magnetic effects (i.e. exchange interactions, finite size effects associated with 2D layers) become important [4, 5]. The competition between multiple interactions places a great challenge on our ability to understand and predict the resulting functional properties, and ultimately to exploit the emergent properties in applications.

In this work, we explore the extent of interfacial interactions occurring in superlattices (SLs) composed of two ferromagnetic (FM) and metallic perovskite oxides, $\text{La}_{0.7}\text{Sr}_{0.3}\text{MnO}_3$

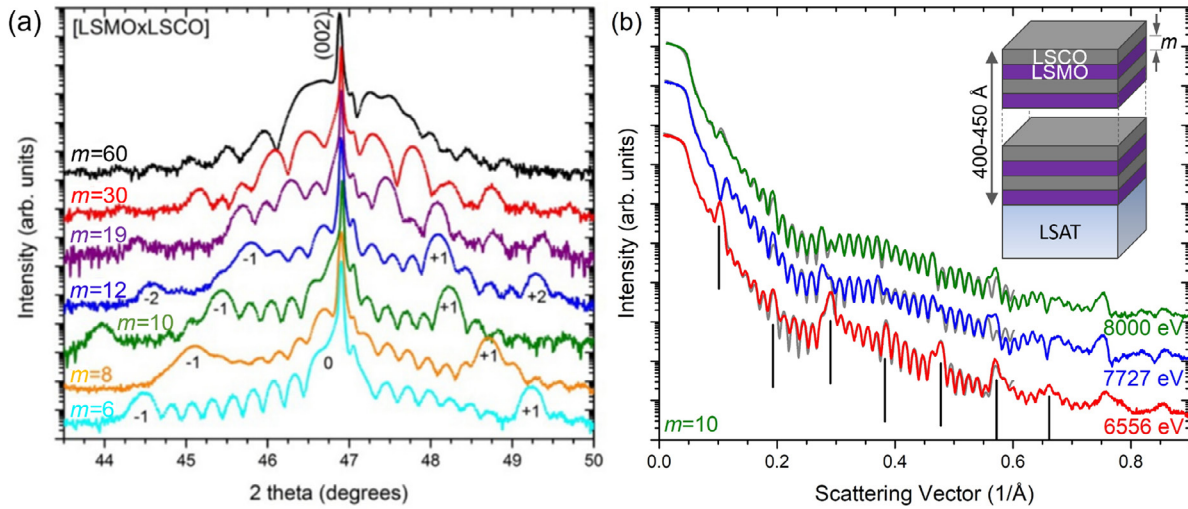


Figure 1. (a) $\omega - 2\theta$ XRD scans of the LSMO/LSCO SLs near the (002) LSAT peak and (b) resonant XRR spectra taken at different x-ray energies for the $m = 10$ LSMO/LSCO SL. Well pronounced SL peaks (denoted as ± 1) and Kiessig fringes were observed for all samples. In (b), the grey lines show fits obtained from Refl1D software corresponding to the parameters listed in table SI. The vertical black lines highlight the SL peaks which appear more prominently at the resonant x-ray energies.

(LSMO) and $\text{La}_{0.7}\text{Sr}_{0.3}\text{CoO}_3$ (LSCO), by varying the sublayer thicknesses from 6 pseudocubic unit cells (u.c.) to 60 u.c. A common Sr-doping level ($x = 0.3$) at the A-site minimizes any A-site chemical intermixing in the heterostructures. LSMO displays a lower coercive field than LSCO [6–8], and the magnetic and electronic properties in both systems are mediated by the double exchange mechanism such that they display simultaneous FM/paramagnetic (PM) and metal/insulator transitions, as well as a peak in magnetoresistance at their Curie temperatures (370 K and 240 K, respectively). As a result, their functional properties are sensitive to changes to the B–O–B bond angles and distances due to epitaxial strain imposed from an underlying substrate [9–11]. At low Sr-doping ($x < 0.18$), the cobaltites $\text{La}_{1-x}\text{Sr}_x\text{CoO}_3$ are characterized by magnetoelectronic phase separation (MEPS) in which nanoscale (~ 25 Å diameter) hole-rich FM clusters exist within a hole-depleted non-magnetic (NM) matrix [12]. The FM cluster size increases as x increases such that at $x = 0.18$, FM magnetic clusters start to coalesce and the material undergoes an insulator/metal transition [6, 13]. It should be noted that for $x > 0.18$, the material does not display pure long range ferromagnetism, but rather exists as a magnetic cluster glass with the NM regions forming a minority volume fraction. This cluster glass phase leads to zero field-cooled (ZFC) and field-cooled (FC) magnetization curves which diverge below the freezing temperature (T_f) [14]. In $\text{La}_{1-x}\text{Sr}_x\text{CoO}_3$ thin films, MEPS dominates near the film/substrate interface leading to insulating, NM behavior for films below a critical thickness, t^* , which ranges from 80 to 300 Å depending on the Sr-doping level and epitaxial strain value [15, 16].

In bulk, both LSMO and LSCO possess rhombohedral symmetry in the $R\bar{3}m$ space group with $a^-a^-a^-$ BO_6 tilt patterns in the Glazer notation [6, 8, 14, 17]. Their rhombohedral lattice parameters are $a(\text{LSMO}) = 5.473$ Å and $\alpha(\text{LSMO}) = 60.42^\circ$ [18] and $a(\text{LSCO}) = 5.416$ Å and $\alpha(\text{LSCO}) = 60.05^\circ$ [6]. However, it has been shown that they respond differently to

epitaxial strain imposed from the underlying substrate. In LSMO thin films, deviations from the bulk $a^-a^-a^-$ BO_6 tilt patterns only persisted for a few unit cells away from the substrate interface [19, 20]. In contrast, for $\text{La}_{0.5}\text{Sr}_{0.5}\text{CoO}_3$ thin films, the BO_6 tilt patterns observed by synchrotron x-ray diffraction (XRD) differed from that of bulk $\text{La}_{0.5}\text{Sr}_{0.5}\text{CoO}_3$ and that of the underlying substrate (NdGaO_3 and $\text{La}_{0.3}\text{Sr}_{0.7}\text{Al}_{0.65}\text{Ta}_{0.35}\text{O}_3$ (LSAT)), and this modified tilt pattern extended throughout the full 100 Å film thickness [21].

We report on the detailed characterization of the structural, magnetic, and electronic properties of LSMO/LSCO SLs as a function of sublayer thickness. In particular, synchrotron radiation-based techniques (e.g. resonant x-ray reflectivity (XRR) and soft x-ray magnetic spectroscopy) were utilized in order to independently probe the magnetic and electronic properties of the individual sublayers. These results demonstrate that interfacial charge transfer in this system extends over distances as large as 5–6 u.c. away from the chemical interface, and results in strong magnetic coupling between the sublayers. For larger sublayer thicknesses, the LSMO and LSCO layers are magnetically decoupled, displaying two independent magnetic transitions with differences in response to temperature and applied magnetic field.

Experimental

The LSMO/LSCO SLs as well as single layer LSMO and LSCO films (~ 300 Å thick) were grown on (001)-oriented LSAT substrates by PLD. The LSMO sublayer was always grown first, such that the top layer of the SLs consisted of an LSCO sublayer. In all cases, an approximately equal number of LSMO and LSCO u.c. were deposited, the thickness of sublayers (m) was varied from approximately 60 u.c. to 6 u.c., and the total film thickness was held between 400–450 Å. The SL notation is $[m(\text{LSMO}) \times m(\text{LSCO})]n$, where n is the number of repeats in the SL. A schematic of the SL structure

Table 1. Summary of average layer thickness (t) and interface roughness (rs) values obtained from resonant XRR fits for the LSMO/LSCO SLs. A full list of fitting parameters is included in table SI.

Sample	Substrate	LSMO		LSCO		Carbon layer	
	rs (Å)	t (Å)	rs (Å)	t (Å)	rs (Å)	t (Å)	rs (Å)
$m = 60$	0.1	224 ± 1	1	199 ± 1	5	17 ± 2	3
$m = 30$	0.1	109 ± 2	2	95 ± 2	4	16 ± 1	3
$m = 20$	0.4	79 ± 1	2	72 ± 4	3	16 ± 1	3
$m = 12$	0.3	41 ± 1	4	38 ± 2	6	16 ± 1	3
$m = 10$	0.2	35 ± 1	3	30 ± 2	4	16 ± 1	2
$m = 8$	3	27 ± 3	3	23 ± 3	7	15 ± 1	3
$m = 6$	2	23 ± 2	4	21 ± 2	5	23 ± 2	4

is shown as the inset to figure 1(b). For simplicity, the SLs will be referred to according to their m value. This design of the SLs maintains a constant volume of LSMO and LSCO within each SL and avoids changes in the epitaxial strain state due to differences in the total film thickness. A KrF ($\lambda = 248$ nm) pulsed laser with 1.2 J cm^{-2} laser fluence and 5 Hz frequency was used, while the substrate temperature and background O_2 pressure were held at 700°C and 0.2 Torr, respectively. The samples were slowly cooled in 300 Torr O_2 pressure after the growth to ensure the proper oxygen stoichiometry of the films. For comparison, a LSMO/LSCO solid solution (i.e. LSCMO) film (~ 60 Å thick) was grown at a substrate temperature of 700°C , and oxygen pressure of 0.2 Torr, by alternating the KrF laser (frequency = 1 Hz and laser fluence = 0.93 J cm^{-2}) between the stoichiometric LSMO and LSCO targets every 4–5 pulses.

Structural characterization was performed using resonant XRR at BL 2–1 of the Stanford Synchrotron Radiation Lightsource (SSRL) and high-resolution XRD using a Bruker D8 Discover four-circle diffractometer with $\text{Cu } K_{\alpha 1}$ radiation ($\lambda = 1.54056$ Å). The resonant XRR measurements [22] were performed at 8000 eV (close to the energy for $\text{Cu } K_{\alpha 1}$ radiation) and at energies near the Mn and Co K edges, at the first inflection point on the rising edge of the x-ray absorption near edge structure spectrum from the sample (i.e. near 6556 eV and 7727 eV, respectively). This technique provides a non-destructive means of determining chemical profiles of multi-layer structures composed of layers with similar density. For these LSMO/LSCO SLs, these chemical profiles consisted predominantly of the Mn/Co ions residing at the B -site of the perovskite structure. The structural parameters (scattering length density, interface roughness, and layer thicknesses) were determined by fitting the resonant XRR spectra at the different x-ray energies simultaneously using the Refl1D software package [23]. The sample models allowed the individual structural parameters of each of the sublayers to vary individually.

The sample magnetization was measured using a superconducting quantum interference device (SQUID) magnetometer with the magnetic field applied along the in-plane [100] substrate direction. Soft x-ray magnetic spectroscopy measurements were performed at beamlines 4.0.2 and 6.3.1 of the Advanced Light Source (ALS). Mn and Co x-ray absorption (XA) spectra were measured in total electron yield (TEY)

mode with the x-rays parallel to the in-plane [100] substrate direction with a 60° angle relative to the surface normal. TEY mode provides surface sensitive information limited by the finite escape depth of secondary electrons (~ 50 Å) and therefore the signal is weighted towards the LSCO and LSMO layers at the top surface of the sample. For SLs with $m > 12$, the signal from the buried LSMO layer cannot be detected. X-ray magnetic circular dichroism (XMCD) was calculated as the difference between two XA spectra taken with right- and left-circularly polarized x-rays with an applied magnetic field ($H = 0.5$ or 1.4 T) applied parallel to the propagation direction of the x-rays. The magnetic field value was chosen to ensure full saturation of the magnetization of all layers in the SLs. Hysteresis loops were measured at a fixed x-ray energy corresponding to the maximum XMCD signal at the Co or Mn L_3 edge. Electrical resistivity measurements were obtained using a Lakeshore Cryogenics TTPX cryogenic probe station in the van der Pauw electrode geometry.

Results and discussion

The structural properties of the LSMO/LSCO SLs were determined using high-resolution XRD and resonant XRR measurements. Figure 1(a) shows the out-of-plane $\omega - 2\theta$ scans around the (002) substrate peak for the series of LSMO/LSCO SLs, while the resonant XRR spectra for the $m = 10$ LSMO/LSCO SL is shown in figure 1(b). A comparison of the spectra for the LSMO/LSCO SLs acquired with x-rays with energies of 6556, 7727, and 8000 eV is shown in figure S1 of the supplemental material (stacks.iop.org/JPhysCM/30/015805/mmedia). Well-defined Kiessig fringes as well as SL peaks (indicated by solid black lines in figure 1(b)) with periodicities corresponding to the expected SL repeat units were observed in all spectra ($\omega - 2\theta$ and resonant XRR), confirming the structural quality of the SLs. Due to resonance effects, the SL peaks become more prominent when the spectra are acquired at the resonant energies [22]. The grey curves correspond to simultaneous Refl1D fits at all three x-ray energies. A thin carbon top layer that formed due to exposure of the samples to x-rays in air is also included to improve the fitting. The full list of fitting parameters is included in table SI, while table 1 summarizes the key parameters. By allowing the structural parameters of each sublayer to vary individually, the fitting reveals that there is asymmetric roughness of the two interfaces in the

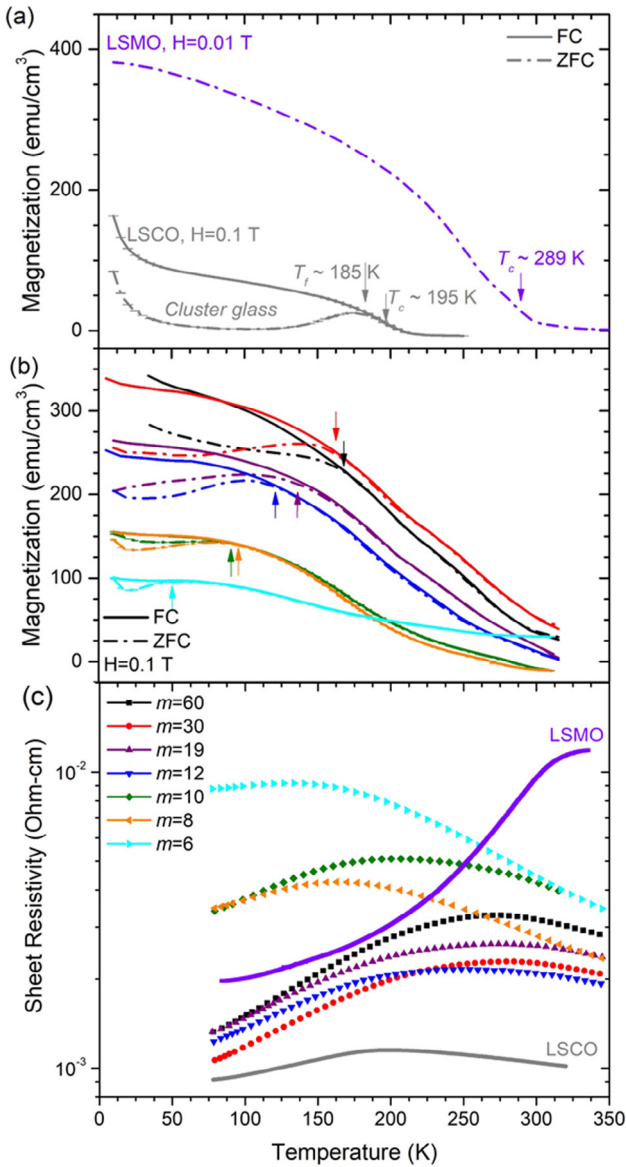


Figure 2. Magnetization as a function of temperature curves for (a) bulk-like LSMO and LSCO films and (b) LSMO/LSCO SLs. Both FC (solid lines) and ZFC (dot-dashed lines) curves are plotted. Arrows denote T_f where the two curves diverge at low temperatures indicating the onset of a cluster glass state. (c) Sheet resistivity as a function of temperature for LSMO and LSCO films and the LSMO/LSCO SLs.

LSMO/LSCO SLs, i.e. in the growth direction, the LSMO/LSCO interface is consistently smoother than the LSCO/LSMO interface. Similar roughness asymmetry was previously reported for the $\text{LaMnO}_3/\text{SrMnO}_3$ and $\text{LaAlO}_3/\text{SrTiO}_3$ systems [24, 25]. Regardless, the chemical roughness of each interface remains below approximately one unit cell thickness, indicating limited chemical intermixing of the sublayers. Reciprocal space maps (figure S2) taken around the $(\bar{1}03)$ and $(\bar{3}03)$ peaks showed that the SLs are fully strained to the underlying LSAT substrate ($a = 3.868 \text{ \AA}$), such that the LSMO (LSCO) sublayers exist under compressive (tensile) strain, respectively.

The temperature dependence of the magnetization of the LSMO/LSCO SLs is plotted in figure 2(b). For comparison,

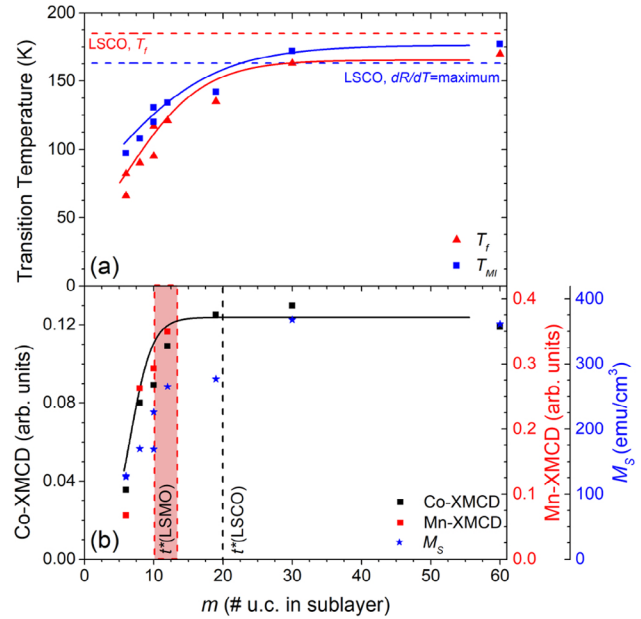


Figure 3. (a) T_f and T_{MI} and (b) magnitude of Co- and Mn-XMCD and M_S measured at 80 K as a function of sublayer thickness for the LSMO/LSCO SLs. The solid lines are guides to the eye, while the horizontal dashed lines refer to data from a bulk-like LSCO film (T_f and T_{MI}). $r^*(\text{LSMO})$ and $r^*(\text{LSCO})$ refer to literature data of the critical thickness below which LSMO and LSCO single layer films display degraded magnetization and conductivity [16, 30–33].

curves for thick, bulk-like ($\sim 300 \text{ \AA}$) LSMO and LSCO single layer films are also plotted (figure 2(a)). Both FC ($H = 0.1 \text{ T}$) and ZFC curves are shown to verify the presence of a cluster glass state in the SLs. The single layer films display nearly-bulk Curie temperature, T_C , values of 289 K and 195 K, for LSMO and LSCO, respectively. T_C was determined as the temperature where $|dM(T)/dT|$ is a maximum. The divergence of the FC and ZFC curves for the LSCO film for temperatures below the freezing temperature, $T_f \sim 185 \text{ K}$, indicates the formation of a cluster glass state [6, 14, 26, 27]. The LSMO/LSCO SLs show the combined characteristics of the LSMO and LSCO films, with two magnetic transitions near 290 and 195 K, as well as a divergence of the FC and ZFC curves below T_f . The magnetic transition for the LSMO sublayers at 290 K appears less abrupt due to the large value of magnetic field ($H = 0.1 \text{ T}$) used to align the hard LSCO sublayers. The T_f values (indicated by vertical arrows in figure 2(b) and plotted as red triangles in figure 3(a)) generally decrease with decreasing LSCO sublayer thickness; for thicker sublayers it decreases gradually, but then decreases more rapidly as the thickness decreases below 10 u.c.'s. As will be discussed further below, the $m = 12$ SL marks the transition between SLs with sublayers with independent, bulk-like properties, and SLs with sublayers dominated by interfacial phenomena.

Since the magnetic properties of both LSMO and LSCO are dictated by the double exchange mechanism, the temperature dependence of the magnetic properties is mirrored in the transport properties shown in figure 2(c). According to this model, the materials undergo a FM/PM transition that coincides with a metal/insulator transition at T_C . The metal/insulator transition temperature, T_{MI} , can be defined as the

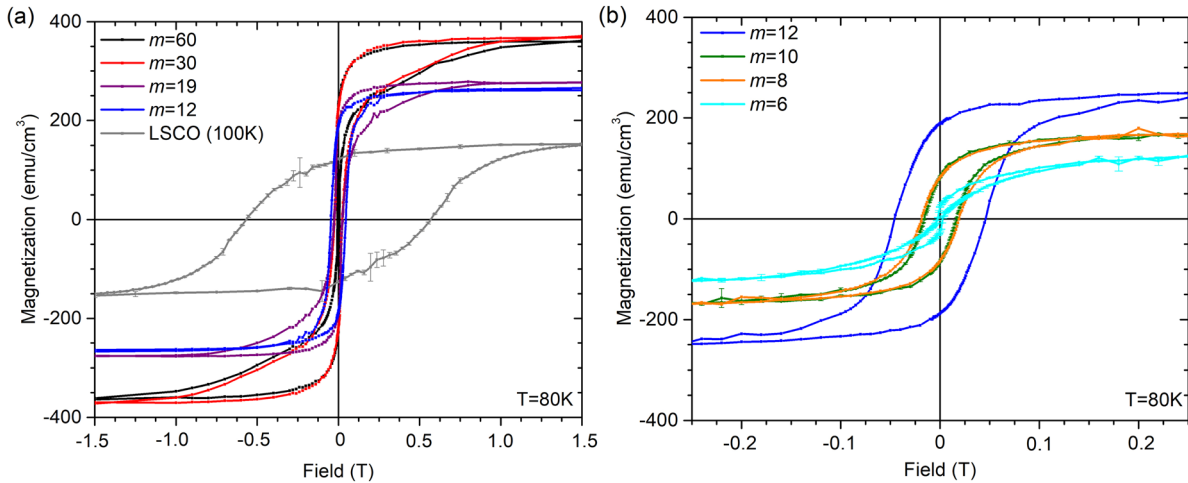


Figure 4. SQUID magnetometry hysteresis loops measured at 80 K for LSMO/LSCO SLs with (a) $m \geq 12$ and (b) $m \leq 12$. For comparison, the data for a thick LSCO film is included in panel (a).

maximum of $|\frac{d\rho(T)}{dT}|$ in analogy to the definition of T_C . This definition leads to $T_{MI} \sim 295$ K and 163 K for the thick LSMO and LSCO films, respectively. For the LSCO film, T_{MI} is slightly lower than the magnetic transition temperature measured by SQUID magnetometry, as has been reported previously [16, 28]. The sublayer thickness dependence of T_{MI} is plotted on figure 3(a) and the values track well with the T_f values extracted from the magnetic properties in figure 2. The shape and values of the resistivity curves for the LSMO/LSCO SLs with $m \geq 12$ are all similar to one another and in reasonable agreement to a parallel resistor model where the current flows proportionally through the LSMO and LSCO layers (see figure S3). In contrast, for the LSMO/LSCO SLs with $m < 12$, a strong deviation away from the parallel resistor model can be seen, with an increase in the low temperature resistivity and a shift of T_{MI} to lower temperatures. It should be noted that even in the limit of the $m = 6$ (thinnest layers) LSMO/LSCO SL, the resistivity behavior is in stark contrast to the LSCO solid solution which showed purely insulating behavior with significantly higher resistivity value (see figure S3; $\rho = 0.43 \Omega \text{ cm}$ at 300 K). This result supports the conclusion of the resonant XRR data of limited chemical intermixing at the LSMO/LSCO interfaces and the formation of a well-defined SL structure. Moreover, these LSMO/LSCO SLs with ultrathin sublayers contrast strongly with ultrathin LSMO and LSCO single layers which also show purely insulating behavior [15, 16, 29–32].

In order to investigate the magnetic coupling between the LSMO and LSCO sublayers, SQUID hysteresis loops were acquired at 80 K (figure 4). For the LSMO/LSCO SLs with $m > 12$ (figure 4(a)), the hysteresis loops are as expected for a composite material composed of two magnetic materials which are decoupled from one another. In this case the two magnetic materials consist of a hard sublayer with large coercivity and small saturation magnetization, M_S (LSCO, $H_C \sim 0.55$ T, $M_S = 150 \text{ emu cm}^{-3}$) and a soft sublayer with small coercivity and large M_S (LSMO, $H_C \sim 0.010\text{--}0.025$ T, $M_S \sim 600 \text{ emu cm}^{-3}$) [6, 8]. For the LSMO/LSCO SLs with $m \leq 12$ (figure 4(b)), only a single magnetic transition was observed

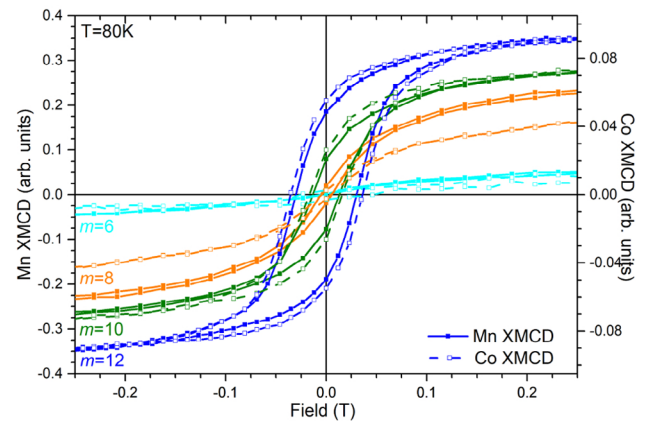


Figure 5. Mn- and Co-XMCD hysteresis loops measured at 80 K for LSMO/LSCO SLs with $m \leq 12$.

despite the fact that the resonant XRR data showed distinct LSMO and LSCO sublayers. For this coupled magnetic phase, H_C and M_S decrease as n increases, following a similar sublayer thickness dependence as seen with the T_f and T_{MI} values shown in figure 3(a). To further examine the coupled nature of the LSMO/LSCO SLs with $m \leq 12$, elemental-specific Co- and Mn- L edge XMCD hysteresis loops are presented in figure 5. The XMCD hysteresis loops allow us to independently probe the magnetic switching of the individual sublayers. In all cases for $m \leq 12$, the Mn- and Co-hysteresis loops coincide with one another with shape, coercivity, and relative magnitudes in good agreement with the SQUID magnetometry data. This agreement between the SQUID and XMCD hysteresis loops confirms that the magnetic behavior of the surface sublayers probed by the XMCD measurements persist throughout the full thickness of the SL. The relative magnitude of the XMCD values scale approximately in a 4:1 ratio of LSMO:LSCO as in their bulk phases [6, 8] and both the Mn- and Co-XMCD values, proportional to the atomic magnetic moment, share the same trend with decreasing sublayer thickness (figure 3(b)). Previous studies on ultrathin $\text{La}_{1-x}\text{Sr}_x\text{CoO}_3$ [15, 16, 29] and LSMO [30–33] films grown on SrTiO_3 (STO) and LSAT substrates have shown a similar abrupt degradation

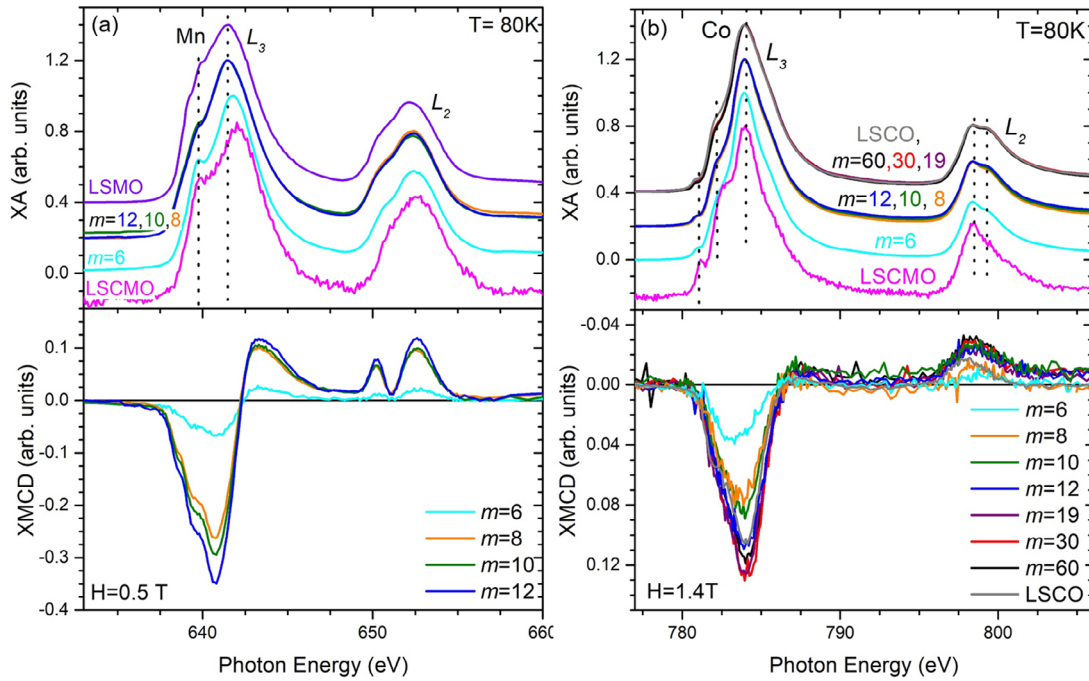


Figure 6. (a) Mn-XA and XMCD spectra; and (b) Co-XA and XMCD spectra for LSMO/LSCO SLs acquired in TEY mode. The somewhat larger noise for the LSCMO solid solution film is due to charging effects related to its insulating behavior at 80 K. The vertical dashed lines indicate the positions of characteristic features in the reference spectra.

in the magnetization and conductivity once the film thickness drops below a critical thickness, t^* . For LSMO films on both types of substrates, t^* was found to be on the order of 10–13 u.c. [30–33], and for LSCO films on LSAT and STO substrates, t^* was 20 u.c. and 39 u.c., respectively [15, 16, 29]. The t^* values for single layer LSMO and LSCO films grown on LSAT substrates are included as vertical dashed lines in figure 3(b). The Mn- and Co-XMCD values show a sharp decrease below $m < 12$ in better agreement with t^* for single layer LSMO films rather than LSCO films.

Rescaling of the T_f and T_{MI} in figure 3(a) in the form of $T'_C(u.c.) = 1 - \frac{T_C(u.c.)}{T_{C,Bulk}}$ shows that as the sublayer thickness decreases, the reduction in transition temperature follows a power law with critical exponent of $\lambda = 0.8 \pm 0.1$ (see figure S4). This exponent is consistent with thickness-dependent data for both single-layer cobaltites [34] and manganites [35], showing that the exchange interaction at the LSMO/LSCO interfaces is on average weaker than the exchange interactions within each sublayer, and this interface coupling becomes significant only when $m < 12$. The much sharper decrease in Co/Mn magnetic moments and total film magnetization with decreasing sublayer thickness (figure 3(b)) illustrates that the average atomic magnetic moment in each sublayer does not change significantly with thickness until the point at which the transition temperature (T_f or T_{MI}) is close to the measurement temperature of 80 K.

XA and XMCD spectra (figure 6) provide further insight into the thickness dependence of the magnetic properties of the LSMO/LSCO SLs, i.e. valence states and local bonding environment for the Mn and Co ions. The Co-XA spectra (figure 6(c)) and Co-XMCD (measured at $H = 1.4$ T, figure 6(d)) for the SLs with $m > 12$ nearly completely overlap

with the spectra from the thick LSCO film, confirming the bulk-like nature of the thick LSCO sublayers. On the other hand, the SLs with $m \leq 12$ show a gradual evolution of the Co-XA spectra from a mixed $\text{Co}^{3+}/\text{Co}^{4+}$ valence state to one which is predominantly Co^{3+} [36–38]. These spectral features are more pronounced at the Co- L_2 edge (shown in detail in figure S5) where there is a gradual decrease in the higher energy B peak of the L_2 doublet feature. This trend towards the Co^{3+} valence state was also observed in ultrathin LSCO films grown on LSAT substrates, and thus may be characteristic of the LSCO/air interface [16]. The shape of the Co-XMCD signal remains largely unchanged for all the LSMO/LSCO SLs with the exception of the $m = 6$ SL which shows a shift in the energy of the maximum Co-XMCD signal to ~ 0.7 eV lower in energy. This result indicates that the FM properties are still mediated by the double exchange mechanism involving $\text{Co}^{3+}/\text{Co}^{4+}$ ions as in bulk LSCO layers. With decreasing LSCO sublayer thickness, the optimal $\text{Co}^{3+}/\text{Co}^{4+}$ network gets broken up by the higher concentration of Co^{3+} ions, thus reducing M_S . The Co-XA and XMCD spectra for the LSCO/LSMO SLs were fit as a linear combination of fundamental spectra from Co^{2+} ions (CoFe_2O_4), Co^{3+} ions (LaCoO_3), and mixed $\text{Co}^{3+}/\text{Co}^{4+}$ ions (LSCO). Figure S6 plots the relative fraction of these fundamental spectra as a function of sublayer thickness, and confirms these trends. In comparison to LSCO/LSAT films, $t^*(\text{LSCO})$ in the LSMO/LSCO SLs has decreased to ~ 12 u.c. from 20 u.c. In contrast, the LSCMO film more closely resembles a mixture of $\text{Co}^{2+}/\text{Co}^{3+}$ valence states with a larger weight on the pre-peak and shoulder features at the Co- L_3 edge. The dominance of magnetically active Co^{2+} ions was also observed in LSCO/LSMO bilayers where the LSCO layer was grown directly on the LSAT substrate, pointing to characteristics of a buried LSCO/LSMO interface [39].

With the TEY measurements, the Mn-XA/XMCD signal emanates primarily from the portion of the LSMO sub-layer in proximity to the top LSMO/LSCO interface, and the signal could not be detected above the noise floor for the $m > 12$ SLs. For the $m \leq 12$ SLs, the interface-sensitive Mn-XA spectra resembles that of the LSCMO film and differs from LSMO single layer films, indicative of a higher $\text{Mn}^{4+}/\text{Mn}^{3+}$ ratio than dictated by the nominal Sr^{2+} doping level. A similar effect has previously been reported for LSMO-based SLs involving LSCO, $\text{La}_{0.7}\text{Sr}_{0.3}\text{FeO}_3$, STO, or LaNiO_3 sub-layers and has been ascribed to an interfacial charge-transfer of the form $\text{Mn}^{3+} + \text{X}^{4+} \rightarrow \text{Mn}^{4+} + \text{X}^{3+}$ or X^{2+} , where X can be Co, Fe, Ti or Ni ions [40–44]. However, as with the Co-XMCD spectra, the spectral shape of the Mn-XMCD curves remains unchanged, indicating that the magnetically active $\text{Mn}^{3+}/\text{Mn}^{4+}$ ions remain largely as in the thick LSMO film though they are broken up by a higher concentration of Mn^{4+} ions. In the case of the LSMO sublayers, $t^*(\text{LSMO})$ remains unchanged in comparison to LSMO/LSAT films.

Based on the characterization results presented above, we have shown that we have grown LSMO/LSCO SLs with high crystalline quality and chemically abrupt interfaces with sub-layer thicknesses which vary from ~ 60 – 6 u.c. The $m = 12$ SL marks the transition between SLs with contrasting magnetic properties. For SLs with $m > 12$, the LSMO and LSCO sub-layers behave independently with bulk-like properties; magnetically soft/metallic LSMO sublayers and magnetically hard/metallic LSCO sublayers with cluster glass characteristics. For SLs with $m \leq 12$, the magnetic and electrical properties of the LSMO and LSCO sublayers are unlike those of either bulk or ultrathin film equivalents or the LSCMO solid solution, and instead are dominated by properties specific to their interfaces. In this regime, LSMO and LSCO sublayers can be characterized as a coupled magnetic phase where the chemically distinct sublayers switch concurrently due to the significant strength of the interfacial exchange interaction as compared to the exchange interaction within each sublayer. Furthermore, the magnetic/electrical parameters of this coupled magnetic phase (e.g. M_s , T_f , T_{MI} , and H_C) can be tailored with the choice of the sublayer thickness. The XA/XMCD spectra suggest that the coupled magnetic properties arise due to an interfacial charge transfer of the form $\text{Mn}^{3+} + \text{Co}^{4+} \rightarrow \text{Mn}^{4+} + \text{Co}^{3+}$, which then promotes a FM exchange coupling vertically across the LSMO/LSCO interface. This effect differs from that seen in LSCO/LSMO bilayers where the LSCO layer was grown directly on the LSAT substrate and magnetic coupling between Co^{2+} and Mn^{4+} ions with large magnetic moment was observed in the XA/XMCD spectra [39]. The vertical extent of this magnetic coupling suggests that the charge transfer extends up to 5–6 u.c. from the interface in either direction, which is in reasonable agreement with numbers quoted in other perovskite systems [36, 39, 45, 46]. This unique behavior of the LSMO/LSCO SLs results due to the differences in electronic characteristics of the Co and Mn ions, and differs to other systems such as the manganite/ruthenate system involving much heavier Ru ions where decoupled properties have been observed down to ultra-thin sublayers [47, 48].

Conclusions

In conclusion, we have performed a detailed investigation of the structural, magnetic, and electrical properties of $\text{La}_{0.7}\text{Sr}_{0.3}\text{MnO}_3/\text{La}_{0.7}\text{Sr}_{0.3}\text{CoO}_3$ SLs as a function of the sub-layer thickness and interface density. The SL with sublayer thickness ~ 12 u.c. marks the transition between SLs in which LSMO and LSCO sublayers are magnetically coupled due to interface exchange interactions; and SLs ($m > 12$) in which the decoupled LSMO and LSCO sublayers have bulk-like properties. These interface effects stem from an interfacial charge transfer of the form $\text{Mn}^{3+} + \text{Co}^{4+} \rightarrow \text{Mn}^{4+} + \text{Co}^{3+}$ which extends approximately 5–6 u.c. from the interface in either direction. In the magnetically coupled state, the magnetic and electronic properties of interest (e.g. M_s , T_f , T_{MI} , and H_C) can be tailored with the choice of the sublayer thickness, despite the fact that the overall SL composition remains unchanged. These findings demonstrate the unique tunability of complex oxides that can result by harnessing interfacial phenomena.

Acknowledgments

This work was supported by the Swiss National Science Foundation (VKM, Grant PBF2-134402) and the Defense Advanced Research Projects Agency (RVC and YT, Grant N66001-11-1-4135). This research used resources of the ALS, which is a DOE Office of Science User Facility under contract no. DE-AC02-05CH11231. Use of the SSRL, SLAC National Accelerator Laboratory, is supported by the US Department of Energy, Office of Science, Office of Basic Energy Sciences under Contract No. DE-AC02-76SF00515.

Supplemental material

The supplemental material includes full structural characterization by resonant XRR measurements and reciprocal space maps, including a full list of the fitting parameters from Refl1D simulations, modeling of the electrical transport measurements using a parallel resistor model, and additional soft XA spectra for the LSMO/LSCO SLs.

ORCID iDs

Rajesh V Chopdekar  <https://orcid.org/0000-0001-6727-6501>
Yayoi Takamura  <https://orcid.org/0000-0002-7946-9279>

References

- [1] Dagotto E 2005 Complexity in strongly correlated electronic systems *Science* **309** 257–62
- [2] Schlom D G, Chen L-Q, Pan X Q, Schmehl A and Zurbuchen M A 2008 A thin film approach to engineering functionality into oxides *J. Am. Ceram. Soc.* **91** 2429–54
- [3] Chambers S A 2010 Epitaxial growth and properties of doped transition metal and complex oxide films *Adv. Mater.* **22** 219–48

- [4] Bhattacharya A and May S J 2014 Magnetic oxide heterostructures *Ann. Rev. Mater. Res.* **44** 65–90
- [5] Chakhalian J, Freeland J W, Millis A J, Panagopoulos C and Rondinelli J M 2014 Colloquium: emergent properties in plane view: strong correlations at oxide interfaces *Rev. Mod. Phys.* **86** 1189–202
- [6] Wu J and Leighton C 2003 Glassy ferromagnetism and magnetic phase separation in $\text{La}_{1-x}\text{Sr}_x\text{CoO}_3$ *Phys. Rev. B* **67** 174408
- [7] Tokura Y 2006 Critical features of colossal magnetoresistive manganites *Rep. Prog. Phys.* **69** 797–851
- [8] Urushibara A, Moritomo Y, Arima T, Asamitsu A, Kido G and Tokura Y 1995 Insulator-metal transition and giant magnetoresistance in $\text{La}_{1-x}\text{Sr}_x\text{MnO}_3$ *Phys. Rev. B* **51** 14103–9
- [9] de Gennes P-G 1960 Effects of double exchange in magnetic crystals *Phys. Rev.* **118** 141–54
- [10] Anderson P W and Hasegawa H 1955 Considerations on double exchange *Phys. Rev.* **100** 675–81
- [11] Millis A J, Littlewood P B and Shraiman B I 1995 Double exchange alone does not explain the resistivity of $\text{La}_{1-x}\text{Sr}_x\text{MnO}_3$ *Phys. Rev. Lett.* **74** 5144–7
- [12] Wu J *et al* 2005 Intergranular giant magnetoresistance in a spontaneously phase separated perovskite oxide *Phys. Rev. Lett.* **94** 037201
- [13] Kuhns P L, Hoch M J R, Moulton W G, Reyes A P, Wu J and Leighton C 2003 Magnetic phase separation in $\text{La}_{1-x}\text{Sr}_x\text{CoO}_3$ by ^{59}Co nuclear magnetic resonance *Phys. Rev. Lett.* **91** 127202
- [14] Senaris-Rodriguez M A and Goodenough J B 1995 Magnetic and transport properties of the system $\text{La}_{1-x}\text{Sr}_x\text{CoO}_{3-\delta}$ ($0 < x < 0.50$) *J. Solid State Chem.* **118** 323–36
- [15] Torija M A *et al* 2011 Chemically driven nanoscopic magnetic phase separation at the $\text{SrTiO}_3(001)/\text{La}_{1-x}\text{Sr}_x\text{CoO}_3$ interface *Adv. Mater.* **23** 2711–5
- [16] Li B, Chopdekar R V, N'Diaye A T, Arenholz E and Takamura Y 2017 Thickness-dependent magnetic and transport properties of epitaxial $\text{La}_{0.7}\text{Sr}_{0.3}\text{CoO}_3$ films *AIP Adv.* **7** 045003
- [17] Ramirez A P 1997 Colossal magnetoresistance *J. Phys.: Condens. Matter* **9** 8171–99
- [18] El-Fadli Z, Metni M R, Sapiña F, Martínez E, Folgado J-V and Beltrán A 2002 *Chem. Mater.* **14** 688–96
- [19] Vaillonis A *et al* 2011 Misfit strain accommodation in epitaxial ABO_3 perovskites: lattice rotations and lattice modulations *Phys. Rev. B* **83** 064101
- [20] Borisevich A Y *et al* 2010 Suppression of octahedral tilts and associated changes in electronic properties at epitaxial oxide heterostructure interfaces *Phys. Rev. Lett.* **105** 087204
- [21] Biegalski M D *et al* 2014 Interrelation between structure—magnetic properties in $\text{La}_{0.5}\text{Sr}_{0.5}\text{CoO}_3$ *Adv. Mater. Interfaces* **1** 1400203
- [22] Kemik N *et al* 2011 Resonant x-ray reflectivity study of perovskite oxide superlattices *Appl. Phys. Lett.* **99** 201908
- [23] Kienzle P A, Krycka J, Patel N and Sahin I (ed) 2011 *ReflID (Version 0.7.7)* (College Park, MD: University of Maryland)
- [24] Nakagawa N, Hwang H Y and Muller D A 2006 Why some interfaces cannot be sharp *Nat. Mater.* **5** 204–9
- [25] May S J *et al* 2008 Magnetically asymmetric interfaces in a $\text{LaMnO}_3/\text{SrMnO}_3$ superlattice due to structural asymmetries *Phys. Rev. B* **77** 174409
- [26] Rata A D, Herklotz A, Nenkov K, Schultz L and Dorr K 2008 Strain-induced insulator state and giant gauge factor of $\text{La}_{0.7}\text{Sr}_{0.3}\text{CoO}_3$ films *Phys. Rev. Lett.* **100** 076401
- [27] Itoh M, Natori I, Kubota S and Motoya K 1994 Spin-glass behavior and magnetic phase diagram of $\text{La}_{1-x}\text{Sr}_x\text{CoO}_3$ ($0 < x < 0.5$) studied by magnetization measurements *J. Phys. Soc. Japan.* **63** 1486–93
- [28] Aargogh H M, Wu J, Wang L, Zheng H, Mitchell J F and Leighton C 2006 Magnetic and electronic properties of $\text{La}_{1-x}\text{Sr}_x\text{CoO}_3$ single crystals across the percolation metal-insulator transition *Phys. Rev. B* **74** 134408
- [29] Torija M A, Sharma M, Fitzsimmons M R, Varela M and Leighton C 2008 Epitaxial $\text{La}_{0.5}\text{Sr}_{0.5}\text{CoO}_3$ thin films: Structure, magnetism, and transport *J. Appl. Phys.* **104** 023901
- [30] Kourkoutis L F, Song J H, Hwang H Y and Muller D A 2010 Microscopic origins for stabilizing room-temperature ferromagnetism in ultrathin manganite layers *Proc. Natl. Acad. Sci.* **107** 11682–5
- [31] Huijben M *et al* 2008 Critical thickness and orbital ordering in ultrathin $\text{La}_{0.7}\text{Sr}_{0.3}\text{MnO}_3$ films *Phys. Rev. B* **78** 094413
- [32] Chopdekar R V, Arenholz E and Suzuki Y 2009 Orientation and thickness dependence of magnetization at the interfaces of highly spin-polarized manganite thin films *Phys. Rev. B* **79** 104417
- [33] Moon E J *et al* 2014 Effect of interfacial octahedral behavior in ultrathin manganite films *Nano Lett.* **14** 2509–14
- [34] Fuchs D, Schwarz T, Moran O, Schweiss P and Schneider R 2005 Finite-size shift of the Curie temperature of ferromagnetic lanthanum cobaltite thin films *Phys. Rev. B* **71** 092406
- [35] de Andres A, Rubio J, Castro G, Taboada S, Martínez J L and Colino J M 2003 Structural and magnetic properties of ultrathin epitaxial $\text{La}_{0.7}\text{Ca}_{0.3}\text{MnO}_3$ manganite films: strain versus finite size effects *Appl. Phys. Lett.* **83** 713–5
- [36] Malik V K, Vo C H, Arenholz E, Scholl A, Young A T and Takamura Y 2013 Magnetic correlation between $\text{La}_{0.7}\text{Sr}_{0.3}\text{MnO}_3$ and $\text{La}_{0.7}\text{Sr}_{0.3}\text{CoO}_3$ layers in artificial superlattices *J. Appl. Phys.* **113** 153907
- [37] Merz M *et al* 2010 X-ray absorption and magnetic circular dichroism of LaCoO_3 , $\text{La}_{0.7}\text{Ce}_{0.3}\text{CoO}_3$, and $\text{La}_{0.7}\text{Sr}_{0.3}\text{CoO}_3$ films: evidence for cobalt-valence-dependent magnetism *Phys. Rev. B* **82** 174416
- [38] Pinta C *et al* 2008 Suppression of spin-state transition in epitaxially strained LaCoO_3 *Phys. Rev. B* **78** 174402
- [39] Li B *et al* 2016 Tuning interfacial exchange interactions via electronic reconstruction in transition-metal oxide heterostructures *Appl. Phys. Lett.* **109** 152401
- [40] Takamura Y, Yang F, Kemik N, Arenholz E, Biegalski M D and Christen H M 2009 Competing interactions in ferromagnetic/antiferromagnetic perovskite superlattices *Phys. Rev. B* **80** 180417
- [41] Li B, Chopdekar R V, Arenholz E, Mehta A and Takamura Y 2014 Unconventional switching behavior in $\text{La}_{0.7}\text{Sr}_{0.3}\text{MnO}_3/\text{La}_{0.7}\text{Sr}_{0.3}\text{CoO}_3$ exchange-spring bilayers *Appl. Phys. Lett.* **105** 202401
- [42] Jia Y *et al* 2016 Thickness dependence of exchange coupling in (111)-oriented perovskite oxide superlattices *Phys. Rev. B* **93** 104403
- [43] Hoffman J *et al* 2016 Oscillatory noncollinear magnetism induced by interfacial charge transfer in superlattices composed of metal oxides *Phys. Rev. X* **6** 041038
- [44] Bruno F Y *et al* 2011 Electronic and magnetic reconstructions in $\text{La}_{0.7}\text{Sr}_{0.3}\text{MnO}_3/\text{SrTiO}_3$ heterostructures: a case of enhanced interlayer coupling controlled by the interface *Phys. Rev. Lett.* **106** 147205
- [45] Ohtomo A, Muller D A, Grazul J L and Hwang H Y 2002 Artificial charge-modulation in atomic-scale perovskite titanate superlattices *Nature* **419** 378–80
- [46] Smadici S *et al* 2007 Electronic reconstruction at $\text{SrMnO}_3/\text{LaMnO}_3$ superlattice interfaces *Phys. Rev. Lett.* **99** 196404
- [47] Ziese M *et al* 2010 Tailoring magnetic interlayer coupling in $\text{La}_{0.7}\text{Sr}_{0.3}\text{MnO}_3/\text{SrRuO}_3$ superlattices *Phys. Rev. Lett.* **104** 167203
- [48] Chen P F *et al* 2013 High- T_C ferromagnetic order in $\text{CaRuO}_3/\text{La}_{2/3}\text{Ca}_{1/3}\text{MnO}_3$ superlattices *Appl. Phys. Lett.* **103** 262402